ART-TOC-ENTRY

Visible light photocatalytic activity of the plasmonic gold–zinc oxide (Au–ZnO) nanorods (NRs) is investigated with respect to the surface defects of the ZnO NRs, controlled by annealing the NRs in ambient at different temperatures.

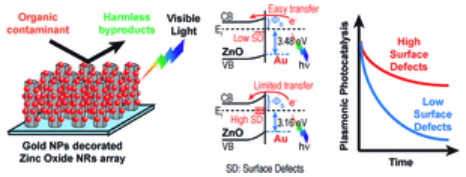

Role of surface defects on visible light enabled plasmonic photocatalysis in Au–ZnO nanocatalysts†

†Electronic supplementary information (ESI) available. See DOI: 10.1039/c5ra16569e

T. Bora,*[a]

M. T. Z. Myint,[a]

S. H. Al-Harthi,[b]

J. Dutta*[a,c]

[a]Chair in Nanotechnology, Water Research Center, Sultan Qaboos University, P. O. Box 17, Al Khoud – 123, Oman. Email: joydeep@kth.SE; tanujjal@squ.edu.om

[b]Department of Physics, College of Science, Sultan Qaboos University, P. O. Box 36, Al Khoud – 123, Oman.

[c]Functional Materials Division, School of Information and Communication Technology, KTH Royal Institute of Technology, Isafjorsgatan 22, SE-164 40 Kista, Sweden.

Abstract

Visible light photocatalytic activity of the plasmonic gold–zinc oxide (Au–ZnO) nanorods (NRs) is investigated with respect to the surface defects of the ZnO NRs, controlled by annealing the NRs in ambient at different temperatures. Understanding the role of surface defects on the charge transfer behaviour across a metal–semiconductor junction is vital for efficient visible light active photocatalysis. Au nanoparticles (NPs) are *in situ* deposited on the surface of the ZnO NRs having different surface defect densities, demonstrating efficient harvesting of visible light due to the surface plasmon absorption. The surface defects in the ZnO NRs are probed by using photoluminescence (PL) spectroscopy, X-ray photoemission spectroscopy (XPS), and photo-electro-chemical current–voltage measurements to study the photo-generated charge transfer efficiency across the Au–ZnO Schottky interface. The results show that the surface situated oxygen vacancy sites in the ZnO NRs significantly reduce the charge transfer efficiency across the Au–ZnO Schottky interfaces lowering the photocatalytic activity of the system. Reduction in the oxygen vacancy sites through annealing the ZnO NRs resulted in the enhancement of visible light enabled photocatalytic activity of the Au–ZnO plasmonic nanocatalyst, adding vital insight towards the design of efficient plasmonic photocatalysts.

Introduction

Photocatalysis by nanostructured metal oxides has been extensively explored in the past due to the potential application in controlling the environmental pollutants for complete mineralization.[1–3] Nanostructured photocatalysts provide

higher surface-to-volume ratios resulting in improved catalytic activity compared to their bulk counterparts. Metal oxides, for example, titanium dioxide (TiO_2), zinc oxide (ZnO), *etc.* are commonly used as photocatalysts, and are typically active under ultra-violet (UV) light due to their wide band gap energies. In recent times, designing photocatalysts that can be activated by visible light is one of the major research areas in order to efficiently and cost-effectively utilize them using the sunlight. Activation of wide bandgap metal oxide photocatalysts under visible light irradiation can be achieved in various ways, among which doping with transition metals,[4–6] creating intermediate defects,[7,8] sensitizing with visible light active dyes or other semiconductors materials,[9–11] narrow bandgap semiconductor coupling[12–14] *etc.* are some of the commonly used methods.

Sensitizing the metal oxide photocatalysts with noble metal NPs to harvest visible light utilizing the surface plasmon resonance (SPR) absorption of the metallic NPs, and hence the name plasmonic photocatalysis, is emerging as a new area for designing smart photocatalysts.[15,16] Plasmonic photocatalysis typically involves distribution of noble metal NPs, like gold (Au), silver (Ag) *etc.* on the surface of semiconductor photocatalysts and thus contains metal–semiconductor junctions in the system.[17,18] Upon activating with visible light, these smart metal–semiconductor plasmonic photocatalysts show several advantages over traditional photocatalysts. Among these, improved visible light harvesting due to the localized SPR absorption and enhanced photo-generated charge separation across the metal–semiconductor interface are primarily important for efficient visible light photocatalytic degradation of pollutants.[16,19]

Recently plasmonic Au–ZnO system has been studied extensively for enhancement of solar cell efficiencies as well as in photocatalysis, for improved visible light harvesting and reduced interfacial charge recombination at the Au–ZnO interface due to the formation of the Schottky barrier at the metal–semiconductor interface.[20–22] However, the formation of the Schottky barrier at the Au–ZnO interface is highly dependent on defects on the semiconductor surfaces. For instance, it has been found earlier that depending on the concentration of surface defect states in ZnO, the Au–ZnO contact behaves either as ohmic or as a Schottky contact.[23,24] Hence understanding the role of surface defects of the semiconductor material on the formation of Schottky barrier at the metal–semiconductor interface and thereby its contribution to the plasmonic photocatalysis by metal–semiconductor photocatalysts is vital.

In the current study, we have modulated the surface defect states of ZnO NRs by annealing the NRs in air at different temperatures and the role of the surface defects of ZnO NRs have been explored in defining the plasmonic photocatalytic performance of Au–ZnO NRs under visible light irradiation. The state of the surface defects in ZnO NRs annealed at different temperatures were explored by photoluminescence (PL) spectroscopy and X-ray photoemission spectroscopy (XPS), whereas the effect of surface defect induced band bending on the formation of Schottky junction upon Au NPs deposition was probed by valence band (VB) XPS measurements. The photo-generated charge transfer and charge separation efficiency across the Au–ZnO Schottky junctions were also explored and discussed from the photo-electro-chemical current–voltage (*I*–*V*) measurements of the Au–ZnO NRs.

Experimental

Synthesis of ZnO NRs

ZnO NRs were grown on glass substrates (3×1 cm^2) by using microwave assisted hydrothermal process.[8] Initially the glass substrates were cleaned subsequently in soap water, acetone, ethanol and de-ionized (DI) water in an ultrasonic water bath. A ZnO seed layer was then deposited on the cleaned glass substrates by spraying 10 ml of 5 mM aqueous solution of zinc acetate at 350 °C. The seeds serve as nucleation sites and enable ZnO NRs to grow preferentially along the *C*-axis of the wurtzite structure during the hydrothermal growth.[25] The seeded substrates were then immersed in a beaker containing an aqueous solution of 20 mM zinc nitrate and 20 mM hexamethylenetetramine. The growth of the NRs was carried out in a commercial microwave oven with microwave output power of 180 W. The hydrothermal growth process of the ZnO NRs consists of two steps: 40 minutes of growth under microwave irradiation and 20 minutes of cooling in the atmosphere. The entire growth process of the ZnO NRs consists of 5 repeated cycles, where the growth solution was replenished in between each cycle in order to maintain a constant growth rate of the NRs during the hydrothermal process. Finally the substrates were retracted from the chemical bath, rinsed thoroughly with DI water followed by drying in an oven at 85 °C for 1 hour and stored until further use.

Deposition of Au NPs on ZnO NRs

Au NPs were deposited *in situ* on the surface of ZnO NRs by photocatalytic reduction of chloroauric acid ($HAuCl_4 \cdot 3H_2O$).[26] In a typical deposition process, ZnO NRs were immersed in a 0.1 mM aqueous solution of $HAuCl_4 \cdot 3H_2O$, followed by irradiation with ultraviolet (UV) light (18 W) for 10 minutes. During the process ZnO NRs absorb the high energy UV light and generate electron–hole (e–h) pairs, which lead to the formation of highly reactive radicals with the subsequent reduction of $AuCl_4^-$ ions to metallic Au on the surface of the NRs. After UV irradiation, the Au–ZnO NRs coated glass substrates were rinsed with copious amount of DI water and dried in air at 85 °C.

Photocatalytic tests

Photocatalysis tests were conducted using an aqueous solution of methylene blue (MB) as a test contaminant with a tungsten-halogen lamp (500 W) as the visible light source. A 10 μM solution of MB was prepared in DI water and placed in poly(methyl methacrylate) (PMMA) cuvettes. A glass substrate containing the ZnO or Au–ZnO NRs was then placed inside the cuvette with the catalyst surface facing the light source. In order to avoid UV and infrared radiation (heat) from the light source a glass vessel (10 cm thick) containing water was placed in between the tungsten-halogen lamp and the cuvettes. The distance between the light source and the cuvette was then adjusted so that the light intensity measured by a

pyranometer (Iso-Tech ISM 410) on the cuvette position is 100 mW cm^{-2}. As a control, a bare glass substrate of similar size was placed in a cuvette containing the MB solution. Optical absorption spectra of the MB solution were then recorded after different light exposure durations in order to monitor the rate of photocatalytic degradation of the test contaminant. Prior to the photocatalytic degradation, the samples were kept in dark for 1 hour in the MB solution to reach adsorption equilibrium. The photocatalytic degradation of MB was estimated from the reduction in absorption intensity of MB at a fixed wavelength λ_{max} = 665 nm and plotted as C_t/C_o *versus* the time of light exposure, where C_t represents the concentration of MB at time t and C_o represents the initial concentration of MB.

Characterization

Surface morphologies of the ZnO and Au–ZnO NRs on glass substrates were characterized by field emission scanning electron microscopy (FESEM; Model: JEOL JSM-7600F) operated at 20 kV. X-ray diffraction (XRD) pattern of the samples were obtained by using a Rigaku MiniFlex600 X-ray diffractometer (Cu Kα radiation, wavelength = 1.54 Å). Optical absorption and photoluminescence (PL) spectra of the samples were recorded by using a Perkin Elmer Lamda 25 UV/Vis spectrometer and Perkin Elmer LS55 fluorescence spectrometer respectively. X-ray photoemission spectroscopy (XPS; Omicron Nanotechnology, Germany) with a monochromatic Al Kα radiation (energy = 1486.6 eV) working at 15 kV was used to study the surface states of the ZnO NRs. The obtained XPS spectra were calibrated with respect to the C 1s feature at 284.6 eV. During the XPS measurements, ZnO samples were flooded with electrons to avoid surface charging during XPS measurements.

Photocurrent measurement in Au–ZnO NRs

In order to study the charge transfer and charge separation efficiency across the Au–ZnO interface with respect to the surface defects of ZnO NRs, Au–ZnO NRs with different surface defects were synthesized on conducting fluorine doped tin dioxide (FTO) substrates as described above. The Au–ZnO NRs on FTO were then used as photoelectrodes and another FTO substrate coated with platinum (Pt) NPs was used as counter electrode to fabricate solar cells by placing the counter electrode facing the photoelectrode. Pt NPs were deposited on the counter electrode by thermal decomposition of 5 mM platinum chloride ($H_2PtCl_6{\cdot}H_2O$) solution prepared in isopropanol at 385 °C for 15 minutes. A single layer of Surlyn 1702 sealant film (50 μm thick) from Dupont, Australia was used as spacer between the two electrodes and the cell was sealed using heat and pressure at the same time. The inter electrode space was then filled with the redox I^-/I_3^- liquid electrolyte, which is composed of lithium iodide (LiI, 0.5 M), iodine (I_2, 0.05 M) and 4-*tert*-butylpyridine (TBP, 0.5 M) dissolved in acetonitrile (ACN). The electrolyte was filled by using capillary force through two small holes (ϕ = 1 mm) drilled on the counter electrode side, which were then sealed by using another piece of Surlyn sealant film. The active area of all the solar cells used in this study was maintained at 0.25 cm^2. The current–voltage (I–V) characteristics of the Au–ZnO solar cells were measured at calibrated 1 sun illumination (AM 1.5G) with intensity equalling to 100 mW cm^{-2}. A Keithley 617 programmable electrometer was programmed with Labview software to act as both voltage supplier and current sensing unit to acquire the I–V characteristics. The fill factor (FF) of the Au–ZnO solar cells was calculated from their I–V curves by using the following equation:

$$\mathrm{FF} = \frac{P_{max}}{P_{th}} = \frac{I_{max} \times V_{max}}{I_{SC} \times V_{OC}}$$

where, I_{SC} is the current produced by the solar cell under short circuit condition, V_{OC} is the open circuit voltage of the solar cell and I_{max} and V_{max} represent the current and voltage values respectively at the maximum power point (P_{max}) which can be delivered by the solar cell to an external load.

Results and discussions

Photocatalytic degradation of MB using Au–ZnO NRs

Morphological characterization by FESEM, as shown in Fig. 1(a), indicates the formation of arrays of ZnO NRs, along with a fairly uniform deposition of Au NPs on the surface of the NRs. The ZnO NRs possess the characteristic hexagonal cross section with diameters ranging from 50 to 100 nm. The inset in Fig. 1(a) shows that the NRs growing perpendicular to the glass substrate that are nearly uniform in length (~4 μm) with a preferential growth direction along the polar facets in the [0002] direction of the ZnO hexagonal wurtzite crystal. Fig. 1(b) shows a typical TEM micrograph of Au–ZnO NRs showing the particle size distribution of the Au NPs. It can be observed that the shape of the as synthesized Au NPs is almost spherical showing a wide distribution of diameters ranging from 7 to 23, which is expected since no capping agents were used during the synthesis of the Au NPs to control their sizes.

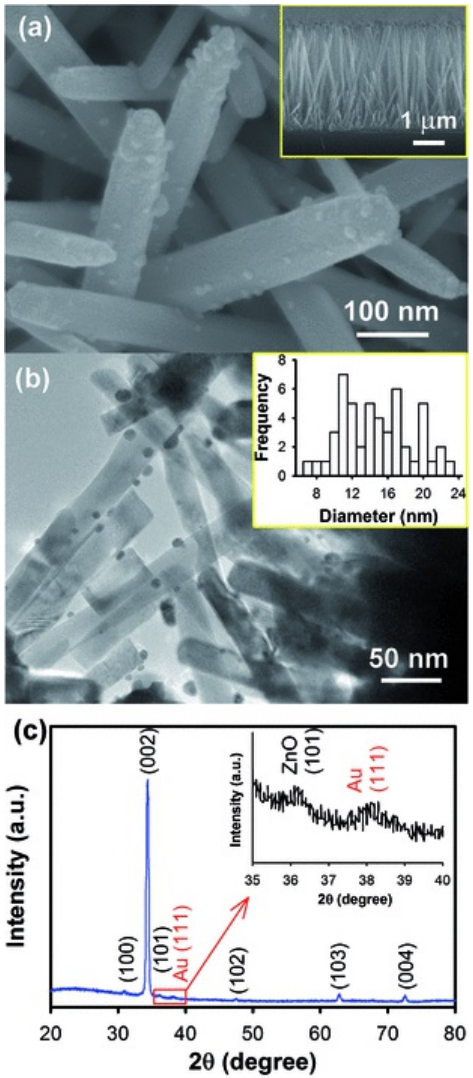

Fig. 1 (a) Typical SEM and (b) TEM micrographs of Au–ZnO NRs showing the Au NPs deposited on the surface of the NRs. Inset in (a) shows the nearly uniform length of the ZnO NRs grown almost perpendicular to the glass substrate and inset in (b) shows the size distribution of the as-deposited Au NPs estimated from 50 particles. (c) XRD pattern of the Au–ZnO NRs and the respective Miller indices. Inset in (c) shows the magnified XRD pattern from diffraction angle (2θ) 35° to 40° of the X-ray diffraction peak from (111) crystal plane of metallic Au NPs at $2\theta = 38.2°$. ZnO NRs were annealed at 450 °C prior to the *in situ* deposition of Au NPs.

Fig. 1(c) shows a typical XRD pattern of the Au–ZnO NRs with their respective Miller indices. The XRD pattern of ZnO NRs, which was verified from JCPDS (Joint Committee on Powder Diffraction Standards) card no. 65-3411, confirms the wurtzite crystal structure of the as prepared ZnO NRs, exhibiting maximum diffraction from (002) crystal plane due to the preferential growth of the NRs along the *C*-axis of the crystal. A small X-ray diffraction peak at 38.2° (magnified as inset) corresponds to the (111) crystal plane of metallic Au (JCPDS card no. 71-4615), confirming the presence of Au NPs in the sample.

Steady state absorption spectra of both ZnO and Au–ZnO NRs exhibited high optical absorption below λ = 380 nm, as shown in Fig. 2(a), due to the high extinction coefficient of ZnO NRs in the UV wavelengths. Compared to the bare ZnO NRs, which displayed lower optical absorption in the visible region (λ > 400 nm), the Au–ZnO NRs showed almost six times higher visible light absorption at ~525 nm, which is characteristic of the surface plasmon resonance (SPR) absorption of Au NPs.[27] An absorption spectrum of colloidal Au NPs is also shown in the inset for comparison. Due to the strong scattering and local field enhancement of light by Au NPs in the near UV region, the absorption band of ZnO NRs

in the Au–ZnO system was also observed to increase slightly. The presence of both UV and visible absorbance maxima for Au–ZnO NRs clearly demonstrates that the material turns photoactive under both UV and visible light irradiation.

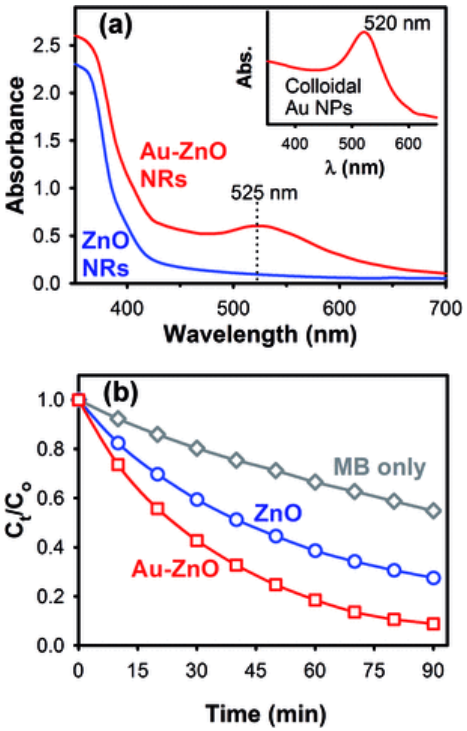

Fig. 2 (a) Steady state room temperature UV/Vis optical absorption spectra of bare ZnO and Au–ZnO NRs and (b) course of photocatalytic degradation of MB under visible light irradiation using bare ZnO and Au–ZnO NRs as photocatalysts. Inset in (a) shows the UV/Vis optical absorption spectrum of colloidal Au NPs showing the SPR peak at 520 nm.

We then compared the photocatalytic degradation of MB as test contaminant under visible light irradiation using bare ZnO and Au–ZnO NRs as photocatalysts, as shown in Fig. 2(b), in order to study the visible light activity of both the systems. In case of the control experiment (in absence of any photocatalysts), the photolysis of MB was observed showing almost 50% reduction in the MB concentration within 90 minutes. In the presence of ZnO NRs, the photocatalytic degradation of MB was observed to occur at a faster rate resulting in almost 50% reduction in MB concentration in less than 40 minutes of visible light illumination. The enhancement in the photocatalytic activity of ZnO NRs under visible light irradiation is mainly due to the presence of the surface defects in the hydrothermally grown ZnO NRs,[8,28,29] which allows sub-bandgap absorption in the material, generating active e–h pairs by absorbing some part of the visible spectrum.[30,31] From the UV/Vis absorption spectra of ZnO NRs (Fig. 2(a)) it can be clearly observed that the optical absorption in ZnO NRs is extended up to the visible region (about 420 nm), indicating the possible presence of surface defects in these NRs and thus making them active under visible light for photocatalytic degradation of MB. The role of surface defects is discussed in details later in this section.

Further enhancement in the photocatalytic degradation of MB was then observed when Au–ZnO NRs were used as photocatalysts due to the improved harvesting of visible light compared to the bare ZnO NRs. All the degradation curve of MB was found to follow a first order exponential equation of the form $y = ae^{-bt}$, where b represents the degradation rate constant of the photocatalytic reduction of MB. 50% reduction in MB concentration in the presence of Au–ZnO NRs was obtained in less than 30 minutes with a rate constant of $2.8 \pm 0.1 \times 10^{-2}$ min^{-1}, demonstrating ~25% higher photocatalytic activity compared to the bare ZnO NRs. Although Au–ZnO NRs show almost six times higher visible light absorption compared to the bare ZnO NRs, the photocatalytic activity of the Au–ZnO NRs under visible light irradiation was found to improve only by about 25% indicating that most of the photo-generated e–h pairs in the Au–ZnO NRs do not actively take part in the photocatalytic reactions. The photocatalytic degradation of MB with Au–ZnO NRs under visible light irradiation occurs through visible light absorption by Au NPs followed by injection of electrons to the conduction band (CB) of ZnO, as explained in Fig. 3. Recently, it has been reported that the quantum efficiency of this injection process in Au–ZnO system is typically very low (in the range of 1–3%),[32] which therefore limits the overall photocatalytic activity of the Au–ZnO NRs in spite of the improved visible light absorption.

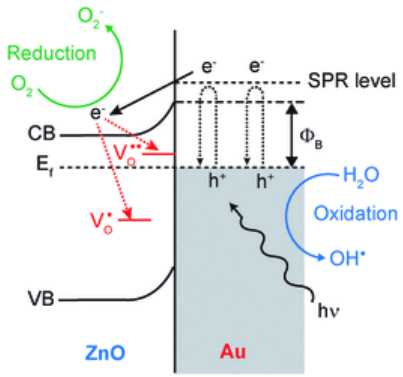

Fig. 3 Energy band diagram of Au–ZnO interface showing the formation of Schottky barrier at the metal–semiconductor interface, where Φ_B is the Schottky barrier potential generated at the Au–ZnO interface, E_f is the Fermi level, while e^- and h^+ are the electrons and holes respectively generated due to photo-excitation of Au NPs. Upon photo-excitation ($h\nu$), e^- injection occurs from the SPR energy level of Au NPs to the conduction band (CB) of ZnO NRs, leaving a photo-generated h^+ in Au NPs separated by the Schottky junction formed at the Au–ZnO interface. $V_O^{\bullet}$ and $V_O^{\bullet\bullet}$ represents oxygen vacancy defect states in ZnO NRs present mostly near the surface acting as e^- trapping sites.

Fig. 3 shows the energy band diagram of Au–ZnO interface showing the electron injection process from photo-excited Au NPs to the CB of ZnO under visible light irradiation. It was reported by several researchers that in the presence of metal NPs in close proximity to semiconductors, as in the case of Au–ZnO NRs, enhanced visible light photocatalytic activity can be observed.[17,22] ZnO, having a wide band gap energy (~3.37 eV), is not a very good visible light photocatalyst and therefore, decoration of ZnO surface with Au NPs enables efficient harvesting of visible light making it visible light active. Additionally, the higher visible light photocatalytic activity for Au–ZnO NRs can also be explained in terms of better separation of the electrons (e^-) and holes (h^+) in the metal–semiconductor composite. It is well known that Au typically forms a Schottky junction with ZnO due to its higher work function (Φ_{Au} ~ 5.3 eV) than the electron affinity of ZnO (~4.2 eV),[24] and hence Au–ZnO NRs can provide higher inhibition towards the recombination of photo-generated charges (back electron transfer) at the Au–ZnO interface. Upon visible light excitation, injection of excited surface plasmons in Au NPs occurs from their SPR energy level to the underlying conduction band (CB) of ZnO, which leaves holes (h^+) at the Au NP side. This process leads to efficient separation of the photo-generated charges across the Au–ZnO Schottky interface,[20] which then undergoes radical formation reactions, as shown in Fig. 3, to take part in the photocatalytic degradation of target pollutants.

The photocatalytic degradation of methylene blue (MB) can occur through both oxidation and reduction processes involving photo-generated e–h pairs that produce highly reactive oxidizing and reducing radicals.[33–35] Since, MB is electroactive and is capable of directly accepting photo-generated e^- from the CB of ZnO, the reduction of MB forming colourless leuco methylene blue (LMB) is predominant during photocatalysis.[36,37] In order to verify this we conducted the photocatalytic degradation of MB using Au–ZnO NRs in the presence of benzoquinone (BQ), which is a well-known e^- acceptor that can efficiently accepts excited e^- from the surface of the Au–ZnO NRs and suppress the formation of O_2^- radicals. Upon addition of BQ, the visible light photocatalytic activity of Au–ZnO NRs was found to reduce significantly (Fig. S1 in ESI†), clearly indicating that photo-generated e^- are the predominant species in the photocatalytic reduction of MB to LMB, which can occur either through O_2^- radical formation or by direct e^- transfer. Additionally the pH of the MB solution during photocatalysis (without BQ) was found to remain in slightly acidic conditions (varying from 6.63 to 6.47), which is also not favourable for oxidation of MB.[38]

Role of surface defects in photocatalytic activity of Au–ZnO NRs

The formation of Schottky barrier at the Au–ZnO interface is affected by several factors, such as surface morphology, surface defects and impurities present on the ZnO surface.[39,40] Amongst these, surface defects have been found to play a major role in defining the properties of the Schottky junction at the Au–ZnO interface.[41] Surface defects in ZnO are mostly present in the form of oxygen vacancy states ($V_O^{\bullet}$ and $V_O^{\bullet\bullet}$), which can act as traps for the injected electrons at the CB of ZnO, as shown in Fig. 3. In order to investigate the role of the surface defects in ZnO on the formation of Schottky junction at the metal–semiconductor interface and thus its effects on the visible light plasmonic photocatalytic activity of the Au–ZnO NRs, we prepared ZnO NRs with different surface defect densities by annealing the NRs in air at different temperatures prior to the deposition of Au NPs. Annealing of ZnO nano-crystals at higher temperatures have been found to alter the concentrations of the defects at the crystal surface.[42–44]

The room temperature PL spectra of ZnO NRs with various surface defect densities are shown in Fig. 4, where all the ZnO NR samples exhibited emission in UV and visible region. The PL bands in the UV region are found to consist of two major components centred at around 370 and 390 nm respectively. The band at ~370 nm (E ~ 3.35 eV) can be correlated to the band-to-band transitions in ZnO representing the bandgap of the material. Another PL component peaking at ~390 nm can originate from non-radiative capture of electrons from the CB of ZnO by defect states situated just below the CB followed by a radiative transition from the defect states to the valence band (VB) of ZnO. In this regard it has been

reported that deep level zinc interstitial (Zn_i) defects, typically situated at ~0.22 eV below the CB of ZnO can be the possible candidate for the violet emission from ZnO.[45] Similarly the broad green-yellow (GY) PL band from the ZnO samples in the visible region was also found to compose of two major components centring at around 510 and 560 nm respectively, typically originating from the surface situated oxygen vacancy states in ZnO.[46,47] The characteristics of each emission band depends on whether it arises from a doubly charged oxygen vacancy center $V_O^{\cdot\cdot}$ (~560 nm) or singly charged oxygen vacancy center $V_O^{\cdot}$ (~510 nm). The doubly charged oxygen vacancies ($V_O^{\cdot\cdot}$), formed by capturing a hole by the $V_O^{\cdot}$ center near the surface, leads to the 560 nm emission band, whereas the singly charged oxygen vacancy ($V_O^{\cdot}$) turns into a neutral center ($V_O^{\times}$) by capturing an electron from the ZnO CB, and the recombination of the electron from the $V_O^{\cdot}$ center to a hole at the ZnO VB results in the 510 nm emission.[48]

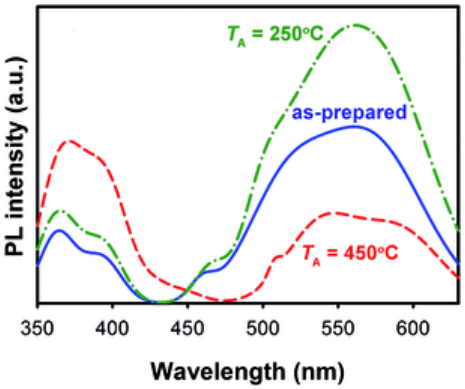

Fig. 4 Room temperature photoluminescence (PL) spectra of as-prepared and annealed (250 °C and 450 °C) ZnO NRs without Au NPs obtained at an excitation wavelength of 325 nm (T_A represents the annealing temperature).

The GY band of the ZnO NRs annealed at 250 °C showed maximum intensity indicating higher concentration of oxygen vacancy sites near the surface of the NRs, compared to the as-prepared ZnO NRs. With temperature, the self-diffusion coefficient of oxygen vacancies in ZnO wurtzite crystal increases; where diffusion occurs mainly through two possible pathways, in which there are six symmetrical paths to the next neighbouring oxygen atoms in the (001) plane (in-plane diffusion) and six equivalent paths with components parallel to the [0001] axis (out-of-plane diffusion).[49] Since in ZnO the axial ratio of the oxygen hcp lattice (c/a = 1.606) is slightly smaller than ideal (c/a = 1.633), the out-of-plane diffusion is dominant allowing the oxygen vacancies to migrate towards the surface of the NRs. As a result, upon annealing, the relative concentration of oxygen vacancy sites gradually increases near the surface, which was found maximum at around 250 °C indicated by the highest intensity of the GY photoluminescence band from ZnO NRs. The compensation of these oxygen vacancies then occurs at the surface through absorption of oxygen from ambient upon further annealing resulting in a reduction of the GY band intensity at 450 °C. In this regard, Wei *et al.*[42,50] have also demonstrated that at annealing temperatures above 300 °C, oxygen vacancies can be eliminated from the ZnO crystal lattice and the Zn–O bonding stoichiometry can be enhanced.

The chemical state of oxygen at the surface of the as prepared and annealed ZnO NRs was further investigated by XPS studies. Fig. 5(a) shows the asymmetric O 1s peaks in the as-prepared and annealed ZnO NRs surface, where the O 1s peak was coherently fitted by three Gaussian components, centred at 530.6 eV (P1), 531.9 eV (P2) and 532.6 eV (P3) respectively. The P1 peak on the lower binding energy side of the O 1s spectrum can be attributed to the O^{2-} ions which are surrounded by zinc atoms with the full supplement of nearest-neighbour O^{2-} ions.[51] Thus, the P1 peak of the O 1s spectrum can be attributed to the Zn–O bonding. The P3 peak towards the higher binding energy at 532.6 eV is usually associated with the chemisorbed or dissociated oxygen or OH species on the surface of the ZnO thin film, such as adsorbed H_2O or adsorbed O_2.[51,52] The middle component at the binding energy 531.9 eV (P2) of the O 1s spectra is related to the O^{2-} ions that are in oxygen-deficient regions within the ZnO matrix (oxygen vacancies).[53,54] Therefore, changes in the area under these peaks upon annealing can be correlated to the variations in the chemical states of oxygen at the surface of the ZnO NRs.

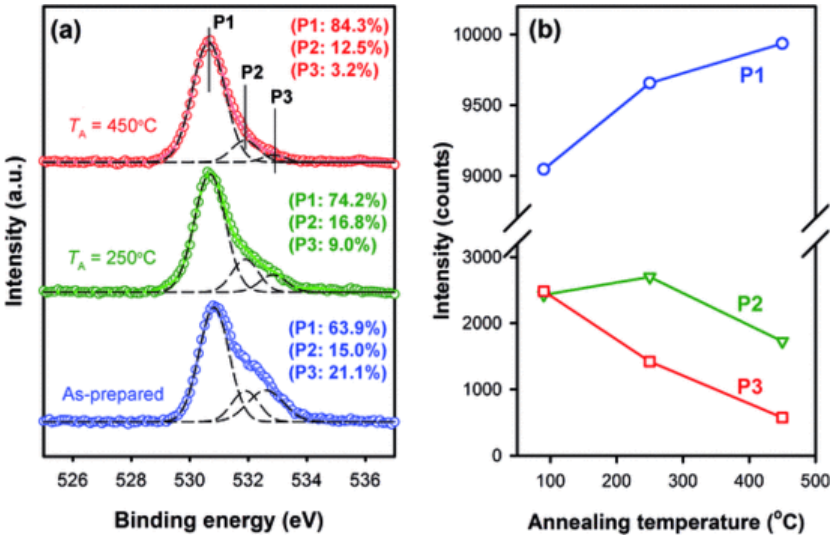

Fig. 5 (a) Oxygen 1s XPS spectra of as-prepared and annealed ZnO NRs (T_A represents annealing temperature). The O 1s spectra were coherently fitted with three Gaussian peaks (P1, P2 and P3) and numbers in parenthesis represent the % area under the deconvoluted peaks. (b) Variations in the absolute intensities of P1, P2 and P3 as a function of the annealing temperature.

The area of the peak P1 was observed to increase continuously (from 63.9% to 84.3%) compared to those of the P2 and P3 peaks, indicating the improvement in the Zn–O bonding in ZnO NRs upon annealing. This is further clearer when absolute intensity of peak P1 was compared between the three ZnO samples, shown in Fig. 5(b), exhibiting continuous improvement in the peak intensity with annealing. Similarly the area under the P3 peak as well as intensity of the P3 peak were observed to decrease constantly, suggesting the reduction of the surface adsorbed species upon annealing. On the other hand, the area of the P2 peak related to the oxygen vacancies was initially observed to increase from 15.0% to 16.8% when NRs were annealed at 250 °C, suggesting accumulation of oxygen vacancy states near the surface of the ZnO NRs. Annealing the ZnO NRs at 450 °C showed reduction in the P2 peak area from 16.8% to 12.5% indicating the removal of the oxygen vacancy sites at 450 °C. A similar trend was also observed in the case of absolute peak intensity of P2 showing maximum intensity for the ZnO NRs annealed at 250 °C, confirming the maximum GY photoluminescence from the 250 °C annealed ZnO NRs as shown in Fig. 4.

In order to probe the effect of the surface defects at the ZnO NRs on the plasmonic photocatalysis of Au–ZnO NRs, photocatalytic degradation of MB was then studied by using Au–ZnO NRs with different surface defect densities. Here Au NPs were *in situ* deposited on the as-prepared and annealed ZnO NRs as explained in the Experimental section. The amount of Au NPs on all the ZnO NRs samples was found to be almost similar, which is confirmed from UV/Vis optical absorptions, as shown in Fig. 6(a). It should be noted that, since Au NPs were *in situ* deposited by photocatalytically reducing $AuCl_4^-$ complex to Au^0 using UV light irradiation and the quantum yield of e–h pair generation in ZnO under UV light irradiation is significantly higher than the yield under visible light; the contribution of surface defects on the photocatalytic reduction of $AuCl_4^-$ complex upon UV light illumination is negligible and amount of Au NPs on the surface of the ZnO NRs can be simply controlled by UV light irradiation time.

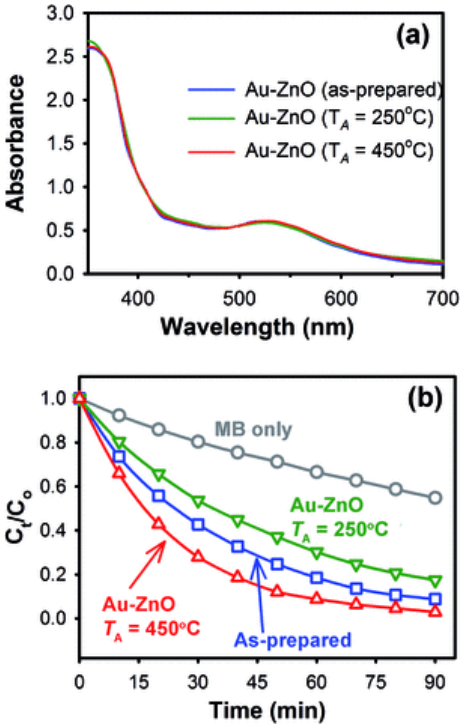

Fig. 6 (a) UV/Vis optical absorption spectra of Au–ZnO NRs showing almost equal amount of Au NPs deposited on the surface of the ZnO NRs in all the samples irrespective of the surface defect densities in ZnO NRs. (b) Plasmonic photocatalytic degradation of MB by the Au–ZnO NRs with different surface defect densities in the ZnO NRs.

The variations in visible light photocatalytic degradation of MB using Au–ZnO NRs with different surface defect densities as photocatalysts is shown in Fig. 6(b). Since the amount of Au NPs is same in all the samples (showing similar visible light absorption spectra), any variations in the photocatalytic activity of the Au–ZnO NRs can be correlated primarily to the charge separation efficiency at the Au–ZnO interface controlled by the Schottky barrier at the interface. It was found that when Au–ZnO NRs were prepared with ZnO NRs having higher surface defects, the plasmonic photocatalytic activity of the Au–ZnO NRs decreases. The photocatalytic rate constant for the Au–ZnO NRs with maximum surface defects in the NRs was obtained as $2.0 \pm 0.2 \times 10^{-2}$ min^{-1}, which was almost 28% slower than the as-prepared Au–ZnO NRs (rate constant: $2.8 \pm 0.1 \times 10^{-2}$ min^{-1}). However, upon reducing the oxygen vacancies by annealing the ZnO NRs at 450 °C followed by formation of Au–ZnO Schottky junctions,[20] the photocatalytic activity was found to improve resulting in highest photocatalytic degradation of MB under visible light with almost 43% enhancement in the degradation rate constant ($4.0 \pm 0.2 \times 10^{-2}$ min^{-1}). The variations in the photocatalytic activity of the Au–ZnO plasmonic photocatalysts can be related to the concentration of the surface situated oxygen vacancy states of ZnO NRs, which has been found to greatly influence the Schottky junction properties at the Au–ZnO NRs by acting as trap states and inducing higher band bending at the surface of the ZnO NRs.

In order to further explore this, we investigated the valence band (VB) XPS spectra of the as-prepared and annealed ZnO NRs which can provide information on the position of the VB with respect to the Fermi level energy (E_f). The aim was to investigate the shift in the VB position due to the surface defects, which can be translated to the shift in the Fermi level (ΔE_f) of ZnO affecting its work function at the surface, and thereby affecting the Schottky barrier height upon deposition of Au NPs on the surface of the ZnO NRs. A common way to measure the work function of ZnO is by using ultraviolet photoemission spectroscopy (UPS) technique.[55] However, it has been shown that UPS measurements frequently results in a reduction in the work function at the nanocrystalline metal oxide surface from its true value due to sample charging and photochemically induced surface modifications, frequently leading to a wrong estimation of the work function.[56] Therefore, in order to avoid such artifacts from UPS measurements, we have estimated the ΔE_{VB} or ΔE_f in terms of $E_f - E_{VB}$ from the VB XPS spectra of the ZnO NR samples. Similar approach has been reported earlier to estimate the VBM of ZnO samples.[57]

Fig. 7(a) shows the VB XPS spectra of the as-prepared and annealed ZnO NRs with different concentrations of oxygen vacancy sites at the surface of the NRs. The strong emission peak observed at binding energy of ~10.5 eV is mainly attributed to the Zn 3d orbital in the ZnO NRs.[57,58] The low intensity peak at binding energy near 5 eV can be attributed to the O 2p orbitals, which is also partially hybridized in the Zn 4s and 4p orbitals.[57] The position of the valence band maximum (VBM) with respect to the Fermi level ($E_f - E_{VB}$) at the surface of the ZnO NRs with different surface defect densities was then estimated from the intersection of the linear fitting of the valence band edge (O 2p emission band). It can

be clearly observed that the VBM of the ZnO NRs annealed at 250 °C, having maximum surface defects, moves closer to the E_f ($E_f - E_{VB}$ = 3.16 eV), compared to the as-prepared NRs ($E_f - E_{VB}$ = 3.22 eV) resulting higher band bending at the surface of the ZnO NRs, as depicted in Fig. 7(b). When the surface defects were minimized by annealing the ZnO NRs at higher temperatures (450 °C), the VBM at the surface of the ZnO NRs was found to move away from the E_f demonstrating $E_f - E_{VB}$ as 3.48 eV. This clearly indicates that upon deposition of the Au NPs on the surface of the ZnO NRs with different surface defect densities, formation of the Schottky junction between Au and ZnO will be affected differently. A higher band bending will result in higher Schottky barrier height at the Au–ZnO interface limiting the photo-generated charge transfer efficiency across the interface. In this regard, it has been reported recently that the Au–ZnO interface annealed at 450 °C possess lowest barrier height (0.67 eV) compared to the samples annealed at 350 °C showing a barrier height of 0.72 eV.[59]

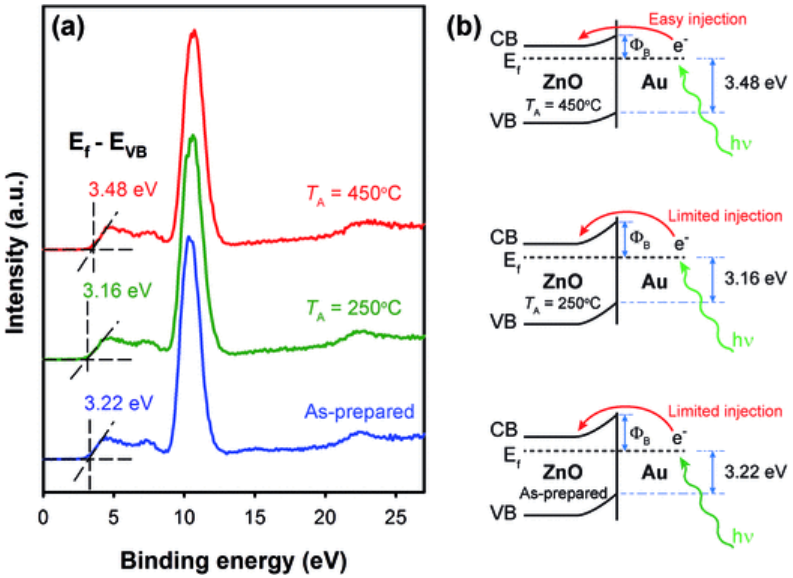

Fig. 7 (a) Valence band (VB) XPS spectra of as-prepared and annealed ZnO NRs showing the Zn 3d spectra, where the intersection shown by dashed line represents the shift in E_{VB} in terms of $E_f - E_{VB}$ at the surface of the ZnO NRs. (b) Band diagram representing the formation of Schottky barrier of different height at the Au–ZnO interface having different band bending (T_A represents annealing temperature).

To explore the photo-generated charge transfer efficiency across the Au–ZnO Schottky interface with different surface defect densities in ZnO NRs, we then studied the current–voltage (*I–V*) characteristics of the Au–ZnO NRs by fabricating solar cells where Au–ZnO NRs were used as photoelectrodes. The photocurrent produced by the solar cells is directly related to the amount of photo-generated electrons injected from Au NPs to the CB of ZnO NRs, whereas the fill factor (FF) of the solar cells can provide direct measure of the losses related to the interfacial charge recombination processes, and thereby giving the charge separation efficiency at the Au–ZnO interface.[20,60,61] Usually higher the photocurrent and FF, higher will be the charge transfer and charge separation efficiency at the Au–ZnO interface respectively, and hence higher will be the photocatalytic activity.

Fig. 8 shows the current–voltage characteristics of the Au–ZnO solar cells, where generation of photocurrent upon light irradiation confirms the injection of the photo-generated e^- from Au NPs to the CB of ZnO NRs, as proposed in Fig. 3. In the case of as-prepared and 250 °C annealed ZnO NRs, very low photocurrent was observed (I_{SC} ~ 15.8 μA cm^{-2}) due to the presence of high concentrations of surface defects resulting in higher band bending, which limits the electron flow from Au NPs to ZnO. Additionally these surface defects also can act as trap sites and capture some of the injected electrons in ZnO side, increasing the interfacial charge recombination indicated by poor FF, which was found to be in the range of 34–36%. On the other hand, when surface defects were reduced by annealing the ZnO NRs at 450 °C, photocurrent of the solar cell was found to increase dramatically (I_{SC} ~ 74.0 μA cm^{-2}) as more electrons could now be injected from Au NPs to the CB of ZnO NRs due to the reduction in the band bending lowering the effective Schottky barrier height at the Au–ZnO interface, as explained in Fig. 7(b). At the same time the FF of the solar cell was also found to improve to ~53% suggesting reduced interfacial charge recombination due to the lowering of the surface situated trap states. These results are consistent with the MB degradation experiments, where maximum visible light photocatalytic activity was observed for the Au–ZnO NRs having minimum surface defects due to the improved photo-generated charge transfer and charge separation efficiency across the Au–ZnO Schottky interface.

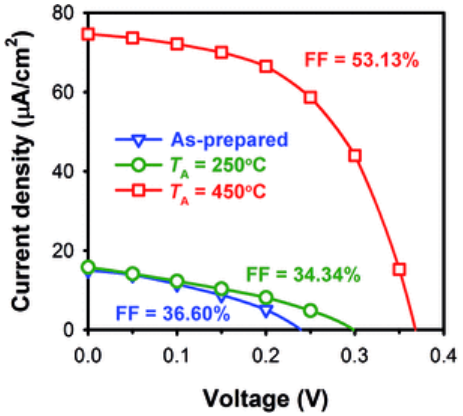

Fig. 8 *I–V* characteristics of Au–ZnO solar cells (active area: 0.25 cm^2). Au NPs were deposited on the surface of ZnO NRs having different surface defect densities and used as photoelectrodes to fabricate the solar cells. T_A represents annealing temperature of ZnO NRs prior to the deposition of Au NPs.

Conclusions

Au NPs decorated ZnO NRs were used to study the plasmonic photocatalysis of Au–ZnO NRs under visible light irradiation. The role of surface defects in the ZnO NRs on the photocatalytic activity of the Au–ZnO NRs was investigated, where the concentrations of the surface defects was controlled by annealing the NRs at different temperatures in air. PL and XPS studies revealed that the surface defects in ZnO NRs are present mostly in the form of oxygen vacancy states and their concentration varies with annealing. The presence of these oxygen vacancy sites at the surface of ZnO NRs was found to be vital in the formation of the Schottky barrier at the Au–ZnO interface upon deposition of the metal NPs. VB XPS analysis of the ZnO NRs and current–voltage measurements in Au–ZnO solar cells demonstrated improved Au–ZnO Schottky junction properties and enhanced charge separation efficiency when the surface defects in ZnO NRs are minimized. The photocatalytic activity of the Au–ZnO NRs studied by degradation of MB as test contaminant under visible light showed almost 43% faster photocatalytic degradation of the dye when the surface defects in ZnO NRs are reduced by annealing the NRs at 450 °C in air, mainly due to the improved harvesting of visible light owing to the surface plasmon absorption of the Au NPs and enhanced charge transfer and charge separation at the Au–ZnO Schottky interface. The results from this study suggest that surface defects in the semiconductor play a crucial role in defining the performance of visible light driven metal–semiconductor based plasmonic photocatalysis.

Acknowledgements

The authors would like to thank the Chair in Nanotechnology, The Research Council of Oman for the financial support to carry out this research work.

Notes and references

1 M. R. Hoffmann, S. T. Martin, W. Choi and D. W. Bahnemann, *Chem. Rev.,* 1995, **95,** 69.

2 A. Mills and S. le Hunte, *J. Photochem. Photobiol., A,* 1997, **108,** 1.

3 A. Mills, R. H. Davies and D. Worsley, *Chem. Soc. Rev.,* 1993, **22,** 417.

4 R. Ullah and J. Dutta, *J. Hazard. Mater.,* 2008, **156,** 194.

5 K. G. Kanade, B. B. Kale, J. O. Baeg, S. M. Lee, C. W. Lee, S. J. Moon and H. Chang, *Mater. Chem. Phys.,* 2007, **102,** 98.

6 T. Fu, Q. Gao, F. Liu, H. Dai and X. Kou, *Chin. J. Catal.,* 2010, **31,** 797.

7 I. Nakamura, N. Negishi, S. Kutsuna, T. Ihara, S. Sugihara and K. Takeuchi, *J. Mol. Catal. A: Chem.,* 2000, **161,** 205.

8 S. Baruah, M. A. Mahmood, M. T. Z. Myint, T. Bora and J. Dutta, *Beilstein J. Nanotechnol.,* 2010, **1,** 14.

9 J. Moon, C. Y. Yun, K. W. Chung, M. S. Kang and J. Yi, *Catal. Today,* 2003, **87,** 77.

10 M. Cheng, W. Ma, C. Chen, J. Yao and J. Zhao, *Appl. Catal., B,* 2006, **65,** 217.

11 S. Sarkar, A. Makhal, T. Bora, K. Lakhsman, A. Singha, J. Dutta and S. K. Pal, *ACS Appl. Mater. Interfaces,* 2012, **4,** 7027.

12 L. Wu, J. C. Yu and X. Fu, *J. Mol. Catal. A: Chem.,* 2006, **244,** 25.

13 J. Liu, R. Yang and S. Li, *Rare Met.,* 2006, **25,** 636.

14 J. Tian, Y. Sang, Z. Zhao, W. Zhou, D. Wang, X. Kang, H. Liu, J. Wang, S. Chen, H. Cai and H. Huang, *Small,* 2013, **9,** 3864.

15 P. Wang, B. Huang, Y. Dai and M.-H. Whangbo, *Phys. Chem. Chem. Phys.,* 2012, **14,** 9813.

16 X. Zhang, Y. L. Chen, R.-S. Liu and D. P. Tsai, *Rep. Prog. Phys.,* 2013, **76,** 046401.

17 F. Pincella, K. Isozaki and K. Miki, *Light: Sci. Appl.,* 2014, **3,** e133.

18 F. Yan, Y. Wang, J. Zhang, Z. Lin, J. Zheng and F. Huang, *ChemSusChem,* 2014, **7,** 101.

19 S. Sarina, E. R. Waclawik and H. Zhu, *Green Chem.,* 2013, **15,** 1814.

20 T. Bora, H. H. Kyaw, S. Sarkar, S. K. Pal and J. Dutta, *Beilstein J. Nanotechnol.,* 2011, **2,** 681.

21 W. He, H.-K. Kim, W. G. Wamer, D. Melka, J. H. Callahan and J.-J. Yin, *J. Am. Chem. Soc.,* 2013, **136,** 750.

22 P. Li, Z. Wei, T. Wu, Q. Peng and Y. Li, *J. Am. Chem. Soc.,* 2011, **133,** 5660.

23 L. J. Brillson, H. L. Mosbacker, M. J. Hetzer, Y. Strzhemechny, D. C. Look, G. Cantwell, J. Zhang and J. J. Song, *Appl. Surf. Sci.,* 2008, **254,** 8000.

24 L. J. Brillson and L. Yicheng, *J. Appl. Phys.,* 2011, **109,** 121301.

25 A. Sugunan, H. C. Warad, M. Boman and J. Dutta, *J. Sol-Gel Sci. Technol.,* 2006, **39,** 49.

26 D. Li, J. T. McCann, M. Gratt and Y. Xia, *Chem. Phys. Lett.,* 2004, **394,** 387.

27 Y. K. Mishra, S. Mohapatra, R. Singhal, D. K. Avasthi, D. C. Agarwal and S. B. Ogale, *Appl. Phys. Lett.,* 2008, **92,** 043107.

28 X. Zhang, J. Qin, Y. Xue, P. Yu, B. Zhang, L. Wang and R. Liu, *Sci. Rep.,* 2014, **4,** 1.

29 Y. Peng, Y. Wang, Q.-G. Chen, Q. Zhu and A. W. Xu, *CrystEngComm,* 2014, **16,** 7906.

30 S. R. A. Raza, Y. T. Lee, Y.-G. Chang, P. J. Jeon, J. H. Kim, R. Ha, H.-J. Choi and S. Im, *Phys. Chem. Chem. Phys.,* 2013, **15,** 2660.

31 R. M. Sheetz, I. Ponomareva, E. Richter, A. N. Andriotis and M. Menon, *Phys. Rev. B: Condens. Matter Mater. Phys.,* 2009, **80,** 195314.

32 A. Pescaglini, A. Martín, D. Cammi, G. Juska, C. Ronning, E. Pelucchi and D. Iacopino, *Nano Lett.,* 2014, **14,** 6202.

33 A. Mills and J. Wang, *J. Photochem. Photobiol., A,* 1999, **127,** 123.

34 Q. Xiang, J. Yu and P. K. Wong, *J. Colloid Interface Sci.,* 2011, **357,** 163.

35 M. Misra, R. K. Gupta, A. K. Paul and M. Singla, *J. Power Sources,* 2015, **294,** 580.

36 L. I. Grossweiner, *Radiat. Res. Rev.,* 1970, **2,** 345.

37 S. Baruah, S. S. Sinha, B. Ghosh, S. K. Pal, A. K. Raychaudhuri and J. Dutta, *J. Appl. Phys.,* 2009, **105,** 0743081.

38 J. M. Bauldreay and M. D. Archer, *Electrochim. Acta,* 1983, **28,** 1515.

39 B. J. Coppa, C. C. Fulton, S. M. Kiesel, R. F. Davis, C. Pandarinath, J. E. Burnette, R. J. Nemanich and D. J. Smith, *J. Appl. Phys.,* 2005, **97,** 103517.

40 H. L. Mosbacker, Y. M. Strzhemechny, B. D. White, P. E. Smith, D. C. Look, D. C. Reynolds, C. W. Litton and L. J. Brillson, *Appl. Phys. Lett.,* 2005, **87,** 012102.

41 L. J. Brillson, H. L. Mosbacker, M. J. Hetzer, Y. Strzhemechny, G. H. Jessen, D. C. Look, G. Cantwell, J. Zhang and J. J. Song, *Appl. Phys. Lett.,* 2007, **90,** 102116.

42 S. Wei, J. Lian and H. Wu, *Mater. Charact.,* 2010, **61,** 1239.

43 Y. Zhang, W. Fa, F. Yang, Z. Zheng and P. Zhang, *Ionics,* 2010, **16,** 815.

44 G. P. Daniel, V. B. Justinvictor, P. B. Nair, K. Joy, P. Koshy and P. V. Thomas, *Phys. B Condens. Matter,* 2010, **405,** 1782.

45 C. H. Ahn, Y. Y. Kim, D. C. Kim, S. K. Mohanta and H. K. Cho, *J. Appl. Phys.,* 2009, **105,** 013502.

46 A. van Dijken, E. A. Meulenkamp, D. Vanmaekelbergh and A. Meijerink, *J. Lumin.,* 2000, **90,** 123.

47 K. Vanheusden, W. L. Warren, C. H. Seager, D. R. Tallant, J. A. Voigt and B. E. Gnade, *J. Appl. Phys.,* 1996, **79,** 7983.

48 J. D. Ye, S. L. Gu, F. Qin, S. M. Zhu, S. M. Liu, X. Zhou, W. Liu, L. Q. Hu, R. Zhang, Y. Shi and Y. D. Zheng, *Appl. Phys. A,* 2005, **81,** 759.

49 P. Erhart and K. Albe, *Phys. Rev. B: Condens. Matter Mater. Phys.,* 2006, **73,** 115207.

50 X. Q. Wei, Z. G. Zhang, M. Liu, C. S. Chen, G. Sun, C. S. Xue, H. Z. Zhuang and B. Y. Man, *Mater. Chem. Phys.,* 2007, **101,** 285.

51 M. Chen, X. Wang, Y. H. Yu, Z. L. Pei, X. D. Bai, C. Sun, R. F. Huang and L. S. Wen, *Appl. Surf. Sci.,* 2000, **158,** 134.

52 S. Major, S. Kumar, M. Bhatnagar and K. L. Chopra, *Appl. Phys. Lett.,* 1986, **49,** 394.

53 P. T. Hsieh, Y. C. Chen, K. S. Kao and C. M. Wang, *Appl. Phys. A,* 2008, **90,** 317.

54 T. Szörényi, L. D. Laude, I. Bertóti, Z. Kántor and Z. Geretovszky, *J. Appl. Phys.,* 1995, **78,** 6211.

55 K. Jacobi, G. Zwicker and A. Gutmann, *Surf. Sci.,* 1984, **141,** 109.

56 S. Gutmann, M. Conrad, M. A. Wolak, M. M. Beerbom and R. Schlaf, *J. Appl. Phys.,* 2012, **111,** 123710.

57 A. G. Joshi, S. Sahai, N. Gandhi, Y. G. R. Krishna and D. Haranath, *Appl. Phys. Lett.,* 2010, **96,** 123102.

58 M. Gabás, S. Gota, J. R. Ramos-Barrado, M. Sánchez, N. T. Barrett, J. Avila and M. Sacchi, *Appl. Phys. Lett.,* 2005, **86,** 042104.

59 J. D. Hwang, F. H. Wang, C. Y. Kung, M. J. Lai and M. C. Chan, *J. Appl. Phys.,* 2014, **115,** 173110.

60 I. Mora-Seró, S. Giménez, F. Fabregat-Santiago, R. Gómez, Q. Shen, T. Toyoda and J. Bisquert, *Acc. Chem. Res.,* 2009, **42,** 1848.

61 A. Alkaya, R. Kaplan, H. Canbolat and S. S. Hegedus, *Renewable Energy,* 2009, **34,** 1595.

Queries and Answers

Query: For your information: You can cite this article before you receive notification of the page numbers by using the following format: (authors), RSC Adv., (year), DOI: 10.1039/c5ra16569e.

Answer: T. Bora, M. T. Z. Myint, S. H. Al-Harthi and J. Dutta, RSC Adv., 2015, DOI: 10.1039/c5ra16569e.

Query: Please carefully check the spelling of all author names. This is important for the correct indexing and future citation of your article. No late corrections can be made.

Answer: Correct

Query: Please check that the inserted Graphical Abstract text is suitable. Please ensure that the text is no longer than 250 characters (including spaces).

Answer: Correct